J. Phys. Chem. A **2008,** *112,* 12220–12227

Conformation-Specific Raman Bands and Electronic Conjugation in Substituted Thioanisoles

Yoshihiro Yamakita,* Tomohiro Okazaki, and Koichi Ohno*

Department of Chemistry, Graduate School of Science, Tohoku University, Aramaki, Aoba-ku,
Sendai 980-8578, Japan

Received: August 6, 2008; Revised Manuscript Received: September 18, 2008

Nonresonant Raman spectra and conformational stability are studied for thioanisole (TA) and substituted analogues [4-XTA, X = NO_2 (**1**), CN (**2**), H (**3**), CH_3 (**4**), and NH_2 (**5**)] at the 4-position. The ring−substituent (SCH_3) vibrational modes of out-of-plane bending and torsional types are calculated to have strong Raman scattering activities only for the vertical conformers. Agreement between observed and calculated Raman spectra is analyzed numerically. The conformational stability of the SCH_3 rotation changes systematically to the electron-withdrawing character of the substituents. The rotational barrier is calculated satisfactorily by B3LYP/6-31++G(d,p) calculations, whereas the second- to fourth-order Møller−Presset perturbation theory and coupled-cluster with single- and double-excitation calculations tend to overestimate conformational energy barriers with respect to coplanar forms. The coplanar form is obtained for **1** and **2**, whereas the vertical conformer is favorable for **4** and **5**. The origin of the conformational energy difference, ΔE, is demonstrated on the basis of canonical molecular orbitals and natural bond orbitals (NBOs) of the ground state. The natural bond orbital interaction between a nonbonding n_S orbital of the S atom and a π orbital of the benzene ring is shown to stabilize the coplanar form predominantly. A linear relationship is obtained between the energy of the highest occupied molecular orbitals and ΔE. The $n_S-\pi$ interaction energy, $E^{(2)}$, based on the NBO representation and the Hammet constants also change linearly with respect to ΔE.

1. Introduction

The conformation of molecules plays an important role in many research fields such as biological sciences and polymer sciences. The microscopic structures of solutions are related to intermolecular interactions involving conformationally fluctuated molecules. The conformational preference has been extensively studied by gas-phase or liquid-phase experiments. In general, low-frequency vibrations including torsional modes give rise to large-amplitude vibrations. They can change the global structure of large molecular systems and will determine the functionality of the system.[1,2] When a molecule undergoes the large-amplitude vibration, a sizable change in its electron distribution is expected.[3] In particular, the vibrational motion induces modulations of electronic interactions between vertically pointing π electrons of aromatic rings and other contacting electrons. Such electronic redistribution will manifest itself as the probability or intensity of optical transitions. The vibrational modes in low-frequency regions can in principle be monitored by optical absorption in the terahertz (far-infrared) region.[1,2,4−6] Such transitions require the electric dipole moment which is apt to localize at local functional groups. On the other hand, Raman scattering reflects polarizability that usually depends upon the volume of electron clouds. Nonpolar functional groups can therefore be monitored, and the additive character of the polarizability would help observation of the global motion.

Raman studies for low-frequency vibrations have long been performed in condensed phases,[7] and experiments using supersonic jets are also possible.[8] However, quantum chemical studies on the Raman intensity have been relatively rare until the recent decade. The electronic rearrangements induced by the large-amplitude vibrations lead to significant Raman scattering activity. On this account, low-frequency modes of various substituents have been studied for substituted benzenes.[9] Heteroatoms in the second and third rows have been introduced at the α-position of the substituents, and variations of the low-frequency modes upon the atomic polarizability[10] and stereochemical structures have been investigated. Nonetheless, the ring−substituent interactions have not been compared for the series of molecules. The potential curve along conformational change is connected with the intramolecular rotation. Those in alkyl-substituted benzenes such as toluene and its derivatives have been studied systematically by electronic spectroscopy experiments using supersonic jets,[11−13] and normal-coordinate analyses have also been reported.[14,15] However, benzene analogues possessing the third-row heteroatoms are yet to be studied, especially by Raman spectroscopy experiments.

Theoretical investigations on the electronic origin of the rotational barrier have been carried out, and systematic correlations have been elucidated in terms of electron distributions,[16] π bond orders,[17] energy density distributions,[18] and hyperconjugations of the $\pi^*-\sigma^*$ type.[19] However, the ring−substituent effects on Raman activity are yet to be studied. The most straightforward analyses of Raman intensity would be those within the polarizability approximation. Orbital interactions such as $\sigma-\pi$ and induced polarizability can be investigated on the basis of the ground-state canonical molecular orbitals. The natural bond orbitals (NBOs), which are defined to give diagonal density matrices, would also be a useful representation,[20,21] since the rotational barriers are known to depend upon the charge distributions.[16,17] The magnitude of NBO interactions can be estimated numerically from the second-perturbation energy, $E^{(2)}$.

In anisole [$C_6H_5O(CH_3)$] and thioanisole [$C_6H_5S(CH_3)$], the substituent in vertical conformers (**v**) sticking out of the benzene

---

* To whom correspondence should be addressed. E-mail: yy@qpcrkk.chem.tohoku.ac.jp (Y.Y.); ohnok@qpcrkk.chem.tohoku.ac.jp (K.O.).

10.1021/jp807027q CCC: $40.75

ring plane is calculated to display marked Raman activities for the low-frequency vibrational modes, whereas coplanar conformers (**p**) with their substituent in the plane show weak Raman activities.[9] The strong Raman activities have been ascribed to interaction between substituent σ electrons and ring π electrons engaged preferentially in the vertical conformers. Thioanisole is known to have a low rotational barrier (5.0 kJ mol^{-1})[22,23] compared to anisole (12.0 kJ mol^{-1}).[24] Although the electronic spectra under jet-cooled conditions[25] and quantum chemical calculations[9,25−27] indicate the coplanar form for thioanisole, vertical conformers could be stabilized upon substitution. The CH_3S substituent is expected to interact electronically with the benzene ring more strongly than the CH_3O substituent. The ionization energy (IE) from the highest occupied molecular orbital (HOMO) is 15.19 eV for CH_3OH, which is far higher than that of benzene, 9.25 eV, whereas that of CH_3SH is considerably close, 12.05 eV.[28] In addition, the wider electron distribution of the S atom would facilitate stronger interaction with the π electrons of the benzene rings. These facts imply the significance of understanding the electronic interactions in thioanisole. The CH_3S group is one of the most important functional groups in the surface sciences.[29]

In this paper we report on Raman activities of the low-frequency modes and conformational stabilizations by conjugation for a series of thioanisoles (TAs) substituted by X = NO_2 (**1**), CN (**2**), H (**3**), CH_3 (**4**), and NH_2 (**5**) (hereafter called 4-XTA or simply X) at the 4-position on the following subjects: (a) variations in the most stable conformer and energy differences of the conformers upon substitution, (b) conformational changes in Raman spectra for each molecule, (c) NBO analyses on orbitals contributing to the stabilization of conformation, and (d) features of polarizability derivatives. The substitution of thioanisole would give a series of different π electron distributions on the benzene ring.

2. Experimental Section

Nonresonant Raman spectra were recorded on a Raman spectrometer (Renishaw, In Via Raman spectromicroscope) at a resolution of 1 cm^{-1} (1800 grooves/mm) with a He−Ne laser for excitation (632.8 nm, 17 mW at the laser front). Low-frequency Raman spectra in the range 10−400 cm^{-1} were recorded using a Rayleigh rejection assembly comprising two gratings (Renishaw NEXT filter). The rejection slits were adjusted carefully for Rayleigh scattered light from a powder sample of sulfur to be deflected completely. Thus, the broad-band tails observed in the low-frequency region mainly originate from thermally populated intermolecular vibrations in the liquids. Electronic absorption spectra were recorded on a UV−vis spectrometer (Hitachi U-2900). All samples of **1**−**5** were obtained as reagent grade material from commercial sources (Aldrich) and were used without purification. The sample sealed in a glass capillary tube was placed at a backscattering geometry. Solid samples (**1** and **2**) at room temperature were heated to melt with a plate heater, and the temperature was monitored by a chromel−alumel thermocouple.

3. Calculations

A. Quantum Chemical Calculations. Density functional calculations were performed with the Gaussian 03 program[30] on Dual-Xeon computers. A parallel computing server (Fujitsu Primequest) at the Research Center for Computational Science of the National Institutes of Natural Sciences was also used partly. Becke's three-parameter gradient-corrected exchange[31] and Lee−Yang−Parr gradient-corrected correlation functionals[32] (B3LYP) were employed for geometry optimization and normal-coordinate and Raman intensity calculations using the 6-31++G(d,p) basis set. Harmonic frequencies were calculated at optimized geometries without scaling. Special care was taken to choose optional parameters for the Gaussian 03 program to avoid computational errors for low-frequency modes; i.e., opt=tight or opt=verytight keywords were specified under int=ultrafine conditions in geometry optimization, and scf=tight was chosen for the SCF calculations with diffuse functions. Symmetry-bound and relaxed calculations were performed carefully in terms of the conformationally flexible substituents. The B3LYP/6-31++G(d,p) level of theory is known[5] to give excellent reproduction (99.0%) of the experimental polarizability of benzene[33] compared to time-dependent Hartree−Fock (HF) theory[34] and calculations using PBE0 functionals.[35]

Ionization energies were obtained from outer valence Green's function (OVGF) calculations based on 6-31++G(d,p). The internal energy at the optimized structures was also calculated by introducing the Møller−Plesset perturbation theory at the second to fourth order (MP2−MP4) and the coupled-cluster method including single and double substitutions with noniterative triple substitution [CCSD(T)]. Such a systematic survey of the theoretical level is necessary for estimating a shallow intermolecular potential energy surface. Especially the conformational stabilization energy of TA has been calculated to be dependent upon the level and basis set employed.[9,23,25−27] The NBO which represents charge distributions explicitly allowed us to estimate orbital interactions. An understanding of the major orbital(s) contributing to the rotational barrier relates to structural control of macromolecules such as biological systems.

B. Accordance Factor. It requires a special treatment to estimate the degree of agreement between experimental and calculated transition intensities, since the results are usually assessed as relative intensity distributions rather than absolute cross sections. Hence, we introduce the accordance factor based on the logarithms of the intensity ratio, $\log(I^{\text{calcd}}/I^{\text{obsd}})$. Details are given elsewhere.[36] Briefly, the reproducibility can be discussed quantitatively by evaluating the root-mean-square, σ, of the logarithm:

$$\sigma = \sqrt{\frac{1}{n}\sum_{i=1}^{n}\left[\log_a\left(\frac{I_k^{\text{calcd}}}{I_k^{\text{obsd}}}\right) - b\right]^2} \tag{1}$$

$$b = \frac{1}{n}\sum_{i=1}^{n}\log_a\left(\frac{I_i^{\text{calcd}}}{I_i^{\text{obsd}}}\right) \tag{2}$$

where I_k^{calcd} and I_k^{obsd} are respectively the kth calculated and observed intensities on an arbitrary linear scale. The logarithmic deviation is converted to the linear scale, and the deviation factor (δ) and the accordance factor (α) are defined respectively as

$$\delta = a^{\sigma} \tag{3}$$

$$\alpha = 1/\delta \tag{4}$$

These indicate that the average accordance of the calculated intensities from the observed intensities is given by the factor α (or $1/\alpha$). α takes values in the range [0, 1] (corresponding to complete disagreement or agreement). Care must be taken when setting a threshold for weak bands that are involved. The observed bands for which relative intensities are less than 0.05 are excluded from the evaluation of α in this work to avoid introducing errors by taking the ratio of weak intensities. Prominent bands are much more important than weak bands.

When the observed spectrum is ascribed to a mixture of two species,[9] A and B, the accordance factor is estimated by assuming superimposition of the species with a weighting ratio x:(1 − x):

$$\sigma(x) = \left\{ \frac{1}{n}\sum_{i=1}^{n}\left[x \log_a\left(\frac{I_i^{\mathrm{calcd,A}}}{I_i^{\mathrm{obsd}}}\right) - xb^{\mathrm{A}} + (1-x)\log_a\left(\frac{I_i^{\mathrm{calcd,B}}}{I_i^{\mathrm{obsd}}}\right) - (1-x)b^{\mathrm{B}} \right]\right\} \quad (5)$$

$$b^{\mathrm{A(B)}} = \frac{1}{n}\sum_{i=1}^{n}\log_a\left[\frac{I_i^{\mathrm{calcd,A(calcd,B)}}}{I_i^{\mathrm{obsd}}}\right] \quad (6)$$

$$\alpha(x) = \frac{1}{a^{\sigma(x)}} \quad (7)$$

where the ratio x is a parameter which takes values in the range [0, 1]. In principle, this definition can be extended to any multicomponents of mixtures. x gives an optimum ratio when α reaches the maximum.

C. Raman Scattering Activity. Nonresonant Raman intensities were calculated on the basis of the polarizability approximation[37] by using a tensor for the quadratic shift of energy (E) in an electric field, which is included in the Gaussian 03 program[30] as a standard option, but polarizability derivatives for modes Q_k were evaluated by the numerical differentiation:

$$\frac{\partial \alpha_{ij}}{\partial Q_k} = \frac{\alpha_{ij}(Q_k + \Delta Q_k) - \alpha_{ij}(Q_k)}{\Delta Q_k} \quad (8)$$

Relative Raman intensities are obtained by multiplying the frequency factor of fourth power of the scattered light (the ν^4 factor) and the thermally weighted amplitude factor [$B_k(T)$] to the Raman scattering activity as[38]

$$I_k \propto (\omega_0 - \omega_k)^4 \frac{1}{\omega_k} S_k(Q_k)\, B_k(T) \quad (9)$$

$$S_k(Q_k) = 45(\alpha_k')^2 + 7(\beta_k')^2 \quad (10)$$

where ω_0 and ω_k are the angular frequencies of the incident light and the kth modes, respectively, S_k is the Raman scattering activity with respect to coordinate Q_k, and B_k is the temperature factor. The temperature factor is derived from the standard Boltzmann factor. For a Stokes transition it is given by

$$B_k(T) = [1 - \exp(-\hbar\omega_k/kT)]^{-1} \quad (11)$$

The Raman scattering activity, $S_k(Q_k)$ (or simply the Raman activity), is obtained in units of $(4\pi\varepsilon_0)^2 a_0^4$/u by converting the output from Gaussian 03.[30] We define the scaled Raman activity $S_k(Q_k)/\tilde{\nu}_k$ in conventional units of $(4\pi\varepsilon_0)^2 a_0^4$/(u cm^{-1}), where $\tilde{\nu}_k$ is the kth vibrational wavenumber in the relation $\omega_k = 2\pi c\tilde{\nu}_k$. It is related to the Raman scattering activity on the basis of the dimensionless normal modes $S_k(q_k)$:

$$S_k(q_k) = \frac{\hbar}{2\pi c\tilde{\nu}_k} S_k(Q_k) \quad (12)$$

4. Results and Discussion

A. Energies of Rotational Isomers. Table 1 summarizes the obtained equilibrium structures (EQs) and transition states (TSs) for 4-NO_2TA (**1**), 4-CNTA (**2**), TA (**3**), 4-CH_3TA (**4**), and 4-NH_2TA (**5**) at the B3LYP/6-31++G(d,p) level of theory. Conformational stability is also compared between the theoretical levels of B3LYP, MP2−MP4, and CCSD(T) on the same basis set, where the energy difference is given with respect to the vertical conformer: $\Delta E = E(\mathbf{p}) - E(\mathbf{v})$. ΔE between the EQ and TS in **1**, **2**, **4**, and **5** corresponds to the rotational barrier. All of the TSs are obtained to be saddle points that give an imaginary frequency along torsional motion.

TABLE 1: EQs and TSs of 4-Substituted TAs 1−5 and Energy Difference [ΔE/(kJ mol^{-1})] with Respect to the Vertical Structures

	1	**2**	**3**	**4**	**5**
coplanar (**p**)[a]	EQ	EQ	EQ	TS	TS
vertical (**v**)[a]	TS	TS	EQ	EQ	EQ
B3LYP/6-31++G(d,p)	−10.6	−9.7	−2.1	0.4	9.1
MP2/6-31++G(d,p)[a]	−1.5	−9.2	5.4	4.3	15.6
MP3/6-31++G(d,p)[a]	−0.5	−12.1	4.9	6.3	16.9
MP4/6-31++G(d,p)[a]	−2.3	−10.1	2.7	3.2	17.5
CCSD(T)/6-31++G(d,p)[a]	−2.3	−7.8	4.2	3.5	17.9
			−2.5[b]		
exptl			−5.0 ± 2.5[b]		

[a] Calculated at the B3LYP/6-31++G(d,p) geometries. [b] Gas electron diffraction. References 22 and 23, respetively.

Qualitatively, the electron-withdrawing substituents NO_2 (**1**) and CN (**2**) stabilize the coplanar structures on the SCH_3 joint bond, whereas the electron-donating CH_3 (**4**) and NH_2 (**5**) groups give the vertical equilibrium structures at the B3LYP/6-31++G(d,p) level of theory. This tendency is unchanged when MP theory or the CCSD(T) method is applied. Full optimization at each level of theory causes little difference in ΔE, indicating minor effects form the optimized structures.

The best agreement with the experimental ΔE of **3** is obtained by the B3LYP/6-31++G(d,p) calculations. Therefore, we hereafter investigate the electronic properties in the ground states obtained from the B3LYP calculations. The electron-withdrawing or -donating characters are not correlated with the calculated OVGF ionization energies for the substituent analogues: HNO_2, 12.32 eV; HCN, 13.43 eV; CH_4, 14.18 eV; NH_3, 9.69 eV. This unmonotonic tendency indicates the importance of orbital mixing through space and eletron correlations.

The significantly negative energy differences for **1** (ΔE = −10.6 kJmol^{-1}) and **2** (−9.7 kJmol^{-1}) indicate their coplanar conformers dominate the thermal population by more than 99% at room temperature, kT = 2.4 kJ mol^{-1}. In contrast, molecule **5** (ΔE = 9.1 kJmol^{-1}) mostly populates in the vertical form by 98%. Molecule **4** is most interesting, which gives **p**:**v** = 49:51 or, in other words, undergoes “free” rotation. We denote these stable conformers **1p**, **2p**, **4v**, and **5v**, respectively.

The value of ΔE hugely depends upon the level of theory. ΔE is calculated significantly larger by the MP and CC methods for all of the cases except for **2**, the deviations being greater than ∼50% of the B3LYP values. The calculated ΔE values of **1** and **3**−**5** at the B3LYP level are systematically more negative by ∼5 kJ mol^{-1} compared to those of the other remaining levels of theory. In general, the B3LYP and CCSD(T) methods normally do not produce an energy difference exceeding ∼10 kJ mol^{-1} for isomerization pathways.[39] However, the present case of ΔE is within or comparable to the accuracy of the calculations. Considering the fact that the B3LYP calculations give the best agreement with the only experimental[22,23] ΔE value of **3**, the obtained discrepancies may stem from the electron correlation treatments by the MP and CC methods. Moreover, the results calculated by these correlation methods display similar disagreements. Thus, the treatments of double and higher excitations in these MO calculations based on the 6-31++G(d,p) basis sets are likely to be responsible for the improper estimation.

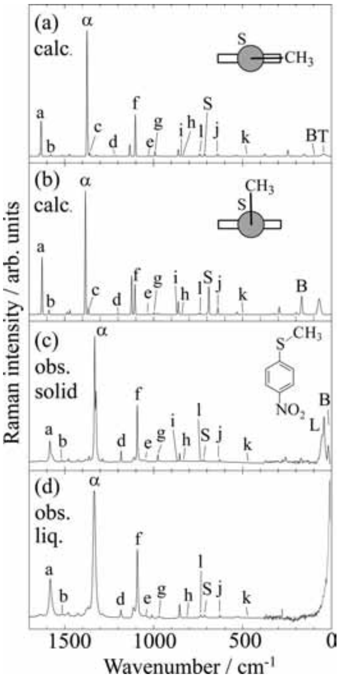

Figure 1. Comparison between calculated Raman spectra of **1** in (a) the coplanar EQ structure and (b) the vertical TS structure and observed Raman spectra at (c) room temperature and (d) 350 K. Key: B, out-of-plane (op) bend of joint S−C; T, torsion around joint S−C; L, lattice vibration; S, S−CH_3 stretch; a, ring 8a; b, ring 8b; c, Kekulé mode (14); d, ring CH in-plane (ip) bend (9a); e, ring 18a; f, half-breathing; g, ring CH op (16a); h, ring CH op (10a); i, ring CH op (11); j, ring 6b; k, ring op (16b); l, ring 6a; α, NO_2 stretch.

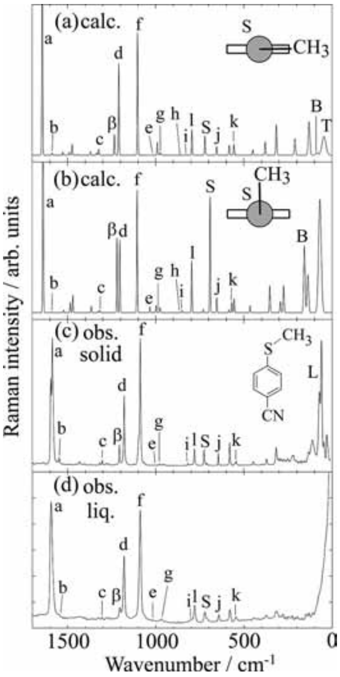

Figure 2. Comparison between calculated Raman spectra of **2** in (a) the coplanar EQ structure and (b) the vertical TS structure and (c) observed Raman spectra at room temperature. For assignments, see the caption of Figure 1. β = ring−CN stretch.

This assumption is supported by the significant basis set dependences found in the calculated conformational barriers involving nonbinding orbital interaction, such as those in thioanisole,[23,25−27] anisole,[26,27,39] glycine,[40,41] and 1,3-benzodioxole.[42] The MP2 method is known to give contradicting ΔE values for thioanisole compared to the experimental ones when moderate basis sets such as 6-311G(d,p) are used.[23] The oscillating behaviors of disagreement at the MP2−MP4 levels shown in Table 1 are similar to those found for the MP2−MP4 calculations for 1,3-benzodioxole with the segmentation-contracted basis sets.[42] Since the limited basis sets cannot describe the diffuse distributions of unoccupied orbitals, the electron correlation representations based on such canonical orbitals are likely to be poor. In particular, the long-range interaction arising from the nonbonding orbitals seems to require large basis sets with higher valences. In contrast, the hybrid B3LYP functionals are relatively immune to the basis sets used, giving satisfactory conformational barriers.[26]

B. Raman Spectra. ***i. 4-Nitrothioanisole (1) and 4-(Methylthio)benzonitrile (2).*** Figures 1 and 2 present observed and calculated nonresonant Raman spectra of **1** and **2**, respectively. The most stable conformers of these analogues are the coplanar form (Table 1). The S_0−S_1 transition energies were determined to be 29 700 and 35 200 cm^{-1} for **1**[43] and **2**, respectively. These energies are sufficiently large compared to the excitation energy of 15 802 cm^{-1}. All Raman bands are normalized to the strongest bands in height and convoluted with a Gaussian bandwidth of 5 cm^{-1} in full width at half-maximum. The temperature factors given in eq 11 are imposed as $B_k(T = 300$ K) on the calculated spectra as the bandwidth. The reasons for this convolution include anharmonicity and intermolecular interactions. The vibrational frequencies are calculated to be slightly higher than the experimental values. As mentioned previously, no scaling factor was used to avoid inconsistency between frequency and normal modes. Assignments can be made straightforwardly on the basis of the calculated intensities and are given as labels in Figures 1 and 2. The complete assignments are given in Table S1 and S2, respectively, in the Supporting Information.

As can be seen in Figures 1a and 2a, ring−substituent bending (B) and torsional (T) vibrations are calculated to be weak for the coplanar form. For the vertical form in Figures 1b and 2b, modes B are obtained to be stronger. The Raman spectra observed for solids at room temperature and liquids at 350 K are also shown in Figures 1 and 2. The bands assigned to lattice vibrations (L) disappear in the liquid-phase spectra, but the rest of the Raman bands are observed similarly. This fact indicates the dominant presence of the coplanar conformers of **1** and **2** in the solid state. All of the doublet bands in Figures 1c and 2c can be assigned to crystal field splitting (Davydov splitting) from the observed single peak in the liquid-phase spectra. Broadband tails are observed from 0 cm^{-1} only in the liquid-phase spectra, which are due to intermolecular vibrations at 350 K.

The accordance factors α given in eq 4 to the coplanar form are 0.78 and 0.63 for **1** and **2**, respectively, which are better than that for **3**, 0.542. The accordance factor $\alpha(x)$ of eq 7 also gives the optimum ratio (x) near the Boltzmann distribution of ΔE. It is noted that the calculated bending mode (B) of the vertical conformer is considerably stronger in Figure 2b. This different behavior is partly due to vibrational coupling with the substituent X. The vertical structures of TS are obtained as first-order saddle points, and imaginary frequencies are obtained along reaction pathways, but such structures could contribute to observation if the structures are fluctuating in liquids.

ii. Methyl p-Tolyl Sulfide (4) and 4-(Methylthio)aniline (5). Figures 3 and 4 show the observed and calculated nonresonant Raman spectra for vertical analogues **4** and **5**, respectively, in their liquid states at room temperature. The calculated results for the TS structures are also shown in Figures 3a and 4a. The TS structure of **4** has an imaginary frequency along its reaction

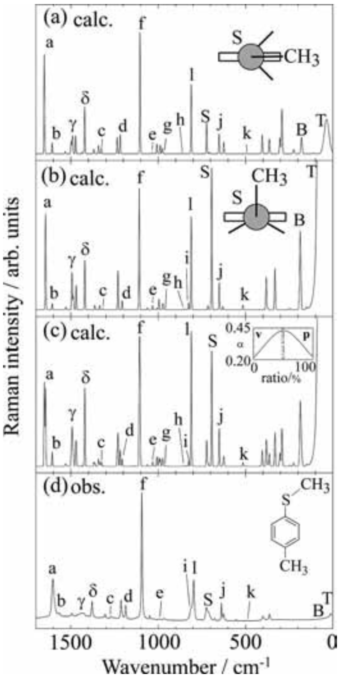

Figure 3. Comparison between calculated Raman spectra of **4** in (a) the coplanar TS structure and (b) the vertical EQ structure, (c) calculated Raman spectra assuming a mixture of coplanar and vertical structures, and (d) observed Raman spectra at room temperature. Inset: accordance factor α as a function of the ratio of coplanar structure. For assignments, see the caption of Figure 1. γ and δ = CH_3 deformations.

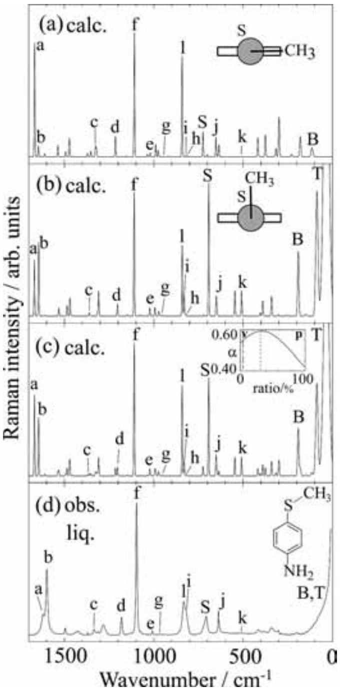

Figure 4. Comparison between calculated Raman spectra of **5** in (a) the coplanar TS structure and (b) the vertical EQ structure, (c) calculated Raman spectra assuming a mixture of coplanar and vertical structures, and (d) observed Raman spectra at room temperature. Inset: accordance factor α as a function of the ratio of coplanar structure. For assignments, see the caption of Figure 1.

pathway to the EQs. The electronic absorptions of **4** and **5** were observed at 385 000 cm^{-1} [44] and 31 900 cm^{-1}, respectively. The vertical conformers of **4** and **5** display surprisingly strong Raman intensities for the ring−substituent modes of B and T in the calculated spectra, in Figure 3a and 4b, respectively. The vibrational amplitudes of the very low-frequency modes of T give rise to the broad bandwidths, and these are overlapped on neighboring bands.

It may seem strange that the observed low-frequency Raman bands for modes B and T of **4** are very weak in Figure 3d compared to the calculations. This disagreement is explained by mixed conformational states over the intramolecular rotation. As shown in Table 1, the shallow rotational barrier of 0.4 kJ mol^{-1} in **4** leads to the free rotation, corresponding to the ratio **p**:**v** = 51:49. To demonstrate this mixing, we synthesize a superimposed spectrum of **4p** and **4v** in proportion to the ratio that maximizes the accordance factor α. The optimum spectra are shown in Figure 3c, and the optimum accordance $\alpha(x)$ with experiment are obtained close to the Boltzmann distributions at 300 K, as shown in the inset. Other evidence of the conformational mixing is the broad widths of Raman bands observed at 724 cm^{-1} (band S) and 797 cm^{-1} (band l). Closely spaced bands are predicted for the coplanar and vertical conformers near these frequencies. Mixing by the conformational fluctuation is responsible for the observed broad bands. These bands cannot be explained on the assumption of pure **4p** or **4v**. Moreover, similar broad bands are not observed for the liquid-phase spectra of **1** and **2**.

Similarly, the ΔE value for **5** yields the Boltzmann distribution, **p**:**v** = 2:98. The synthesized Raman spectrum for **5** leads to the maximum accordance factor $\alpha(x)$ shown in the inset of Figure 4c. The resultant optimum ratio, 36:64, is slightly deviated. This discrepancy may demonstrate a limit of the superimposed spectra and/or the calculated ΔE. In addition, strong Raman bands are not observed for modes B and T in Figure 4d in contrast to the predicted spectrum. Possible reasons include that the observed board long tail near 0 cm^{-1} is overlapped on bands B and T. Strong intermolecular interactions such as hydrogen bonding could also be present in the liquid. Again, the broad bands are observed, at 706 cm^{-1} (band S) and 833 cm^{-1} (band l). Since the vibrational modes of S and l involve SCH_3 stretching and C−S stretching, respectively, these are sensitive to the conformational change. The assignments for **4** and **5** are summarized in Tables S3 and S4, respectively, in the Supporting Information, assuming the vertical conformers.

As shown in Figure 3, the methyl group in **4** is calculated to be in the same symmetry plane of the SCH_3 group. Thus, the rotational barrier of CH_3 is involved in the **4p**−**4v** energy difference, but the rotational barrier of CH_3 has been reported to be only ~0.1 kJ mol^{-1} for *p*-fluorotoluene.[11] This small value allows us to disregard that conformational contribution to ΔE. As mentioned below, the para substitution effect estimated by the Hammet constant[45] for F ($\sigma_p = 0.06$) is very close to that of SCH_3 ($\sigma_p = 0.00$).[46]

C. Orbitals Contributing to Conformational Stability. It is known that the electron-withdrawing or electron-donating character of functional groups is characterized quantitatively by the Hammet constant (σ_p for para substitution).[45,46] The Hammet constant is an empirical constant which represents the preference of deprotonation for the para- or meta-substituted benzene analogues having the functional group in question. The parameters are widely used in determining the mechanisms of organic reactions and analyzing reaction rates. Physical parameters such as ionization energy and bond dissociation enthalpy are known to show linear relations with the Hammet constants.[47] The substituted thioanisoles in this work are also found to show a linear relation for ionization energies with the Hammet constants, as shown in Figure 5. The plotted ionization energies were determined by the OVGF/6-31++G(d,p) calculations for

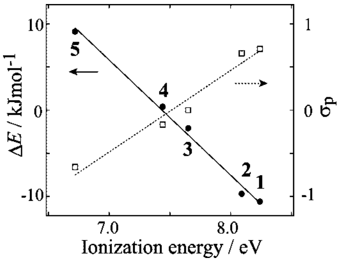

Figure 5. Energy difference $\Delta E = E(\mathbf{p}) - E(\mathbf{v})$ and Hammet constants σ_p as a function of ionization energy (IE) for **1**−**5**.

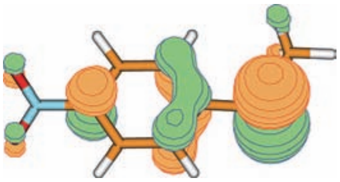

Figure 6. HOMO orbital of the coplanar conformer of **1**.

the coplanar conformers. No linear relations were obtained for other orbital energies except that of the HOMOs. This fact implies the dominant role of the HOMOs in the coplanar structures in conformational stabilization. This assumption is supported by another linear relation of ΔE as a function of IE, also shown in Figure 5. Figure 6 depicts the HOMO of **1p**, showing mixing between a nonbonding orbital, n_S, of the S atom and a benzene π orbital. Since the n_S orbital extends off-axially from the joint bond of SCH_3, it can interact with the π orbital only in the coplanar form. However, the picture of the HOMO gives only a qualitative understanding of this orbital interaction.

D. Natural Bond Orbital Analyses. The natural bond orbital allows us more quantitative analyses for the orbital interactions, especially when charge transfer is involved. The magnitude of orbital mixing can be estimated by the second-order stabilization energy, $E^{(2)}$, which is given by[20,21]

$$E^{(2)} = q_i \frac{F(i,j)^2}{E(j) - E(i)} \tag{13}$$

where q_i is the electron occupancy of a donor orbital, $F(i,j)$ is an off-diagonal component (i, j) of the Fock matrix, and $E(i)$ and $E(j)$ are the orbital energies of the ith donor NBO and jth acceptor NBO, respectively. If the $n_S-\pi$ interaction is a dominant factor to determine the conformational stability ΔE, $E^{(2)}$ is expected to correlate directly with ΔE. The major natural bond orbitals which interact with each other in each conformation are depicted in Figure 7. In the coplanar form, the n_S donor orbital and π acceptor orbital in Figure 7a interact predominantly, whereas in the vertical form the σ_{SMe} orbital, n_S orbital, and σ_{BZ} orbital play a major role.

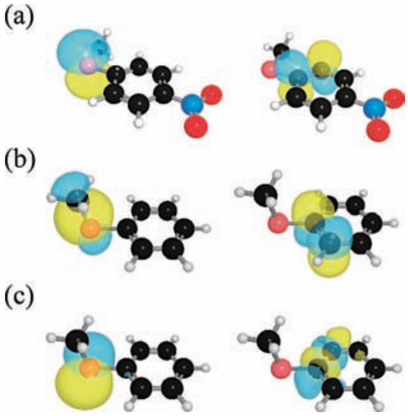

Figure 7. Interacting NBOs: (a) nonbonding n_s donor orbital at S and π acceptor orbital on the benzene ring in coplanar **1**, (b) σ_{SMe} orbital along the SCH_3 bond and π orbital on the benzene ring in vertical **3**, and (c) nonbonding n_S orbital at S and σ_{BZ} orbital of the benzene ring in vertical **3**.

TABLE 2: Interaction Energies $E^{(2)}$ of Natural Bond Orbitals in the Coplanar Form (Type I) and Vertical Form (Types II and III)

type	interaction (D−A)	$E^{(2)}$/(kJ mol^{-1})				
		1	2	3	4	5
I	$n_S-\pi$	−89.5	−86.2	−78.1	−76.1	−70.1
II	$n_S-\sigma_{BZ}$	−37.5	−37.5	−36.7	−37.2	−37.8
III	$\sigma_{SMe}-\pi$	−9.7	−10.0	−10.9	−11.3	−12.5
II + III		−47.2	−47.5	−47.6	−48.5	−50.3

Table 2 lists interaction energies $E^{(2)}$ of the major natural bond orbitals in the coplanar form (I) and vertical form (II and III). As expected, $E^{(2)}$ indicates the most significant stabilization energy for the $n_S-\pi$ interaction of type I in the coplanar form. The other interactions of types II and III, which are most facilitated in the vertical form, are found to be small in magnitude. In particular, type III is 3 or 4 times smaller than type II. Therefore, the $\sigma_{SMe}-\pi$ interaction is not very strong within the representations of the natural bond orbitals. Figure 8 plots the tendency of $E^{(2)}$ as a function of ΔE. The obtained linearity for the type I interaction gives additional support to the stabilization mechanism. The interactions of types II and III in the vertical forms display little change without linearity. The ionization energies used in Figures 5 and 8 are those of the coplanar form, which is connected with their HOMOs of the $n_S + \pi$ type.

The strong Raman activities of the vibrations involving SCH_3 are preferentially obtained in the vertical form, as shown in Figures 1−4. On the other hand, the $\sigma_{SMe}-\pi$ interaction, which

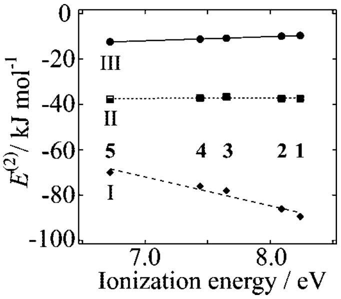

Figure 8. Interacting energy $E^{(2)}$ between natural bond orbitals as a function of ΔE: type I, nonbonding n_s orbital at S and π orbital on the benzene ring; type II, σ_{SMe} orbital along the SCH_3 bond and π orbital on the benzene ring; type III, nonbonding n_S orbital at S and σ_{BZ} orbital of the benzene ring.

TABLE 3: Calculated Static Dipole Polarizability $(4\pi\varepsilon_0 a_0^3)$[a]

molecule	α_{xx}	α_{xy}	α_{xz}	α_{yy}	α_{yz}	α_{zz}	α_{iso}
1p	66.18	0.00	0.00	120.57	−9.03	198.86	128.53
2p	67.04	0.00	0.00	108.95	−8.54	198.11	124.70
3p	62.87	0.00	0.00	105.17	−7.22	138.57	102.20
3v	72.13	0.00	8.67	99.60	0.00	131.56	101.10
4v	81.49	0.00	10.11	108.23	0.00	156.33	115.35
5v	78.24	0.00	9.76	105.19	0.00	160.61	114.68

[a] Calculated at the B3LYP/6-31++G(d,p) level for **1**−**5**, where **p** = coplanar and **v** = vertical. The molecule fixed axes are defined in the directions of x, out-of-plane, y, short axis of the ring, and z, long axis of the ring.

TABLE 4: Polarizability Derivatives with Respect to the Bending and Torsional Modes [$4\pi\varepsilon_0 a_0^3$ (u cm^{-1})$^{-1/2}$][a]

mode	$\tilde{\nu}$/cm^{-1}	molecule	$\partial\alpha_{ij}/\partial q_k$					
			xx	*xy*	*xz*	*yy*	*yz*	*zz*
bending	91	**1p**	0.029	−0.017	0.064	−0.001	−0.006	−0.016
	86	**2p**	0.033	−0.009	−0.093	0.018	0.001	0.021
	170	**3p**	0.020	0.010	−0.118	0.019	−0.002	0.025
	117	**3v**	0.047	0.000	−0.274	−0.005	0.000	−0.185
	187	**4v**	−0.032	0.000	0.197	0.014	0.000	0.189
	192	**5v**	−0.020	0.000	−0.113	−0.011	0.000	−0.244
torsional	43	**1p**	0.028	0.130	−0.034	−0.009	−0.012	0.006
	45	**2p**	0.025	0.133	−0.090	0.022	−0.003	0.017
	40	**3p**	0.032	0.141	−0.083	0.040	−0.002	0.025
	15	**3v**	−0.028	0.783	−0.003	−0.021	0.206	−0.044
	13	**4v**	0.040	−0.630	−0.012	0.071	−0.077	0.080
	35	**5v**	0.013	−0.492	−0.003	0.012	−0.129	0.028

[a] Calculated at the B3LYP/6-31++G(d,p) level for **1**−**5**, where **p** = coplanar and **v** = vertical. The large components in the modulus are underlined. The molecule fixed axes are defined in the directions of *x*, out-of-plane, *y*, short axis of the ring, and *z*, long axis of the ring.

is most likely to be modulated by the low-frequency modes B and T, gives a weak $E^{(2)}$ value in Table 2. However, the small $E^{(2)}$ value does not necessarily mean a small *modulation*. The energy difference $E(j) - E(i)$ was calculated to be comparable to that of type I interaction. The small off-diagonal matrix element $F(i,j)$ is found to be responsible for this small $E^{(2)}$ value of the $\sigma_{\mathrm{SMe}}-\pi$ interaction. Hence, the vibrational modulation could still be induced by the $\sigma_{\mathrm{SMe}}-\pi$ interaction through the spatial interaction of both orbitals since $F(i,j)$ is expected to be sensitive to geometrical change. When the SCH_3 bond approaches the π electron distributions, only the orbital overlap of type III is anticipated to be modulated. Quantitative evidence for this modulation can be verified by evaluating $E^{(2)}$ at displaced geometries. Their contribution to the Raman intensity is obtained using the formalism of the second-order energy gradient of $E^{(2)}$ in electric fields (eq 5 in ref 9). The present calculations merely present static orbital interactions under field-free conditions.

E. Polarizability and Polarizability Derivatives. Table 3 shows calculated polarizability tensors. To compare the ring−substituent interactions, the molecular fixed axes (x, y, z) are converted from the principal axes of inertia to those which are parallel or perpendicular to the substituent axes. The definitions of the axes are the following. The z-axis points to the direction connecting the diagonal C atoms connecting the substituents, the y-axis is located in a plane spanned by the z-axis and the line connecting the midpoints of the CC bonds parallel to the z-axis, and the x-axis points to the out-of-plane direction defined by the x- and y-axes. The polarizabilities of **1**−**5** are calculated to be anisotropic. The largest diagonal polarizability elements are obtained in the long-axis direction of the ring (z-axis) as expected, whereas the smallest ones are in the out-of-plane direction (x-axis). Among these molecules, **1** and **5** are calculated to have the largest polarizability in long-axis (z) diagonal elements. This trend is likely connected with the number of bonds stemming ffom the α atom of the 4-position. Increasing the bond lengths or the number of bonds (electrons) involved generally leads to expanded electron clouds that give rise to large polarizabilities.

Table 4 presents the polarizability derivatives with respect to the dimensionless normal coordinates q_k for the bending and torsion modes. The large amplitude of vibrational motion is thus reflected in these derivatives. As underlined in Table 4, the large polarizability change by the bending and torsional modes can be found in the off-diagonal components of the *xz* and *xy* planes, respectively. These components clearly indicate the remarkable Raman enhancement for **3v**, **4v**, and **5v**. In addition, the small diagonal elements indicate that the volume changes of electron distributions are small in these non totally symmetric vibrational modes. The *xz* and *xy* components of polarizability derivatives are induced in the plane on which the low-frequency modes take place. The natural populations[48] of electrons condensed to the atoms do not explain the propensity of the polarizability change. Hence, the polarizability changes are likely to be caused by the delocalized electrons rather than the simple movement of the localized charges. The obtained conformation-dependent Raman intensities for the bending modes could be due to additive polarizability from the vertical SCH_3 bond in motion. However, those for the torsional modes cannot be explained by this additive effect. This enhancement is thus connected with the electronic conjugation interactions between the σ electrons and π electrons. It is noted that the magnitudes of the off-diagonal components become smaller on going away from the coplanar or vertical **3**. This propensity is opposite the order of the diagonal polarizability such as α_{zz} in Table 3.

5. Conclusion

The bending and torsional modes are calculated to display strong Raman activities preferentially in the vertical conformers of substituted thioanisoles. The rotational barrier highly correlates with the energy levels of the HOMOs. The natural bond orbitals of n_S and π types interact with each other most strongly and give rise to the stabilization of coplanar conformers. That is, the substituents possessing heteroatoms with nonbonding orbital(s) can in principle stabilize the coplanar conformation through the $n_S-\pi$ interaction in any molecule. It would be even possible to stabilize a desired conformer or to obtain Raman intensities for the bending mode. Although the rotational barrier has been studied extensively as mentioned previously, few quantum chemical studies have been performed in connection with Raman intensities, especially by using the representation of natural bond orbitals. This work demonstrates that the $n_S-\pi$ interaction plays a major role in the conformational stabilization on the basis of the self-consistent-field canonical orbitals. However, interactions involving higher unoccupied orbitals are also likely to contribute.[18,19] Further studies taking into account excitations of the π, σ, or n orbitals seems to be necessary. It is noted that the $n_S-\pi$ interaction involving the nonbonding orbital is not modulated by the large amplitude motion. Thus, the $\sigma_{\mathrm{SMe}}-\pi$ interaction is still a candidate for the strong Raman intensities observed for the low-frequency modes, since these vibrational modes are also strongly observed in aromatic hydrocarbons.[15,49] In principle, contributions from each molecular orbital or natural bond orbital can be evaluated when the polarizability derivatives are obtained using the numerical differentiation (eq 9) with the finite field method.[50] The resonance Raman effect can also be investigated by taking into account the electronic excitations.

Acknowledgment. This work was supported by a Grant-in-Aid for Scientific Research (C) (No. 19550002, 2007) from the Japan Society for the Promotion of Science.

Supporting Information Available: Numerical data of observed and calculated Raman spectra. This material is available free of charge via the Internet at http://pubs.acs.org.

References and Notes

(1) Lin, S. W.; Groesbeek, M.; Hoef, I.; Verdegem, P.; Lugtenburg, J.; Mathies, R. A. *J. Phys. Chem. B* **1998**, *102*, 2787.

(2) Gervasio, F. I.; Cardini, G.; Salvi, P. R.; Schettino, V. *J. Phys. Chem. A* **1998**, *102*, 2131.

(3) Borodin, A.; Yamazaki, M.; Kishimoto, N.; Ohno, K. *J. Phys. Chem. A* **2005**, *110*, 1783.

(4) Ferguson, B.; Zhang, X.-C. *Nat. Mater.* **2002**, *1*, 26.

(5) Johnston, M. B.; Herz, L. M.; Khan, A. L. T.; Köhler, A.; Davies, A. G.; Linfield, E. H. *Chem. Phys. Lett.* **2003**, *377*, 256.

(6) Chen, Y.; Liu, H.; Deng, Y.; Schauki, D.; Fitch, M.; Osiander, R.; Dodson, C.; Spicer, J. B.; Shur, M.; Zhang, X.-C. *Chem. Phys. Lett.* **2004**, *400*, 357.

(7) Blatz, L. A. *J. Chem. Phys.* **1967**, *47*, 841.

(8) Hartland, G. V.; Henson, B. F.; Venturo, V. A.; Hertz, R. A.; Felker, P. M. *J. Opt. Soc. Am. B* **1990**, *7*, 1950.

(9) Yamakita, Y.; Isogai, Y.; Ohno, K. *J. Chem. Phys.* **2006**, *124*, 104301.

(10) Donald, K. J. *J. Phys. Chem. A* **2006**, *110*, 2283.

(11) Okumura, K.; Mikami, N.; Ito, M. *J. Phys. Chem.* **1985**, *89*, 5617.

(12) Zhao, Z.; Parmenter, C. S.; Moss, D. B.; Bradley, A. J.; Knight, E. W.; Owens, K. G. *J. Chem. Phys.* **1992**, *96*, 6362.

(13) Fujii, M.; Takezawa, K.; Ito, M. *Spectrochim. Acta, A* **1994**, *50*, 1421.

(14) Moss, D. B.; Parmenter, C. S.; Ewing, G. E. *J. Chem. Phys.* **1987**, *86*, 51.

(15) Ohno, K.; Kimura, J.; Yamakita, Y. *Chem. Phys. Lett.* **2001**, *341*, 207.

(16) Sonoda, Y.; Iwata, S. *Chem. Phys. Lett.* **1995**, *243*, 176.

(17) Lu, K.-T.; Weinhold, F.; Weisshaar, J. C. *J. Chem. Phys.* **1995**, *102*, 6787.

(18) Kawamura, Y.; Nakai, H. *Chem. Phys. Lett.* **2003**, *673*, 368.

(19) Nakai, H.; Kawai, M. *J. Chem. Phys.* **2000**, *113*, 2168.

(20) Reed, A. E.; Weinhold, F. *J. Chem. Phys.* **1983**, *78*, 4006.

(21) Glendening, E. D.; Badenhoop, J. K.; Reed, A. E.; Carpenter, J. E.; Bohmann, J. A.; Morales, C. M.; Weinhold, F. *NBO 5.0*; Theoretical Chemistry Institute, University of Wisconsin: Madison, 2001.

(22) Zaripov, N. M. *Zh. Strukt. Khim.* **1976**, *17*, 741; *J. Struct. Chem. (Engl. Transl.)* **1976**, *17*, 640.

(23) Shishkov, I. F.; Khristenko, L. V.; Karasev, N. M.; Vilkov, L. V.; Oberhammer, H. *J. Mol. Struct.* **2008**, *873*, 137.

(24) Spellmeyer, D. C.; Grootenhuis, P. D. J.; Miller, M. D.; Kuyper, L. F.; Kollman, P. K. *J. Phys. Chem.* **1990**, *94*, 4483.

(25) Nagasaka-Hoshino, M.; Isozaki, T.; Suzuki, T.; Ichimura, T.; Kawauchi, S. *Chem. Phys. Lett.* **2008**, *457*, 58.

(26) Bossa, M.; Morpurgo, S.; Stranges, S. *J. Mol. Struct.: THEOCHEM* **2002**, *618*, 155.

(27) Bzhezovskii, V. M.; Kapustin, E. G. *Russ. J. Org. Chem.* **2002**, *38*, 564.

(28) Kimura, K.; Katsumata, S.; Achiba, Y.; Yamazaki, T.; Iwata, S. *Handbook of HeI Photoelecron Spectra of Fundamental Organic Molecules*; Japan Scientific: Tokyo, 1981.

(29) Maksymovych, P.; Dougherty, D. B. *Surf. Sci.* **2008**, *602*, 2017.

(30) Frisch, M. J.; Trucks, G. W.; Schlegel, H. B.; Scuseria, G. E.; Robb, M. A.; Cheeseman, J. R.; Montgomeri, J. A., Jr.; Vreven, T.; Kudin, K. N. ; Burant, J. C.; Millam, J. M.; Iyengar, S. S.; Tomasi, J.; Barone, V.; Mennucci. ; Cosi, M.; Scalmani, G.; Rega, N.; Petersson, G. A.; Nakatsuji, H.; Hada, M.; Ehara, M.; Toyota, K.; Fukuda, R.; Hasegawa, J.; Ishida, M.; Nakajima, T.; Honda, Y.; Kitano, O.; Nakai, H.; Klene, M.; Li, X.; Knox, J. E.; Hratchian, H. P.; Cross, J. B.; Adamo, C.; Jaramillo, J.; Gomperts, R.; Stratmann, R. E.; Yazyev, O.; Austin, A. J.; Cammi, R. ; Pomelli, C.; Ochterski, J. W.; Ayala, P. Y.; Morokuma, K.; Voth, G. A.; Salvador, P.; Dannenberg, J. J.; Zakrzewski, V. G.; Dapprich, S.; Daniels, A. D.; Strain, M. C.; Farkas, O.; Malick, D. K.; Rabuck, A. D.; Raghavachari, K.; Foresman, J. B.; Ortiz, J. V.; Cui, Q.; Baboul, A. G.; Clifford, S.; Cioslowski, J.; Stefanov, B. B.; Liu, G.; Liashenko, A.; Piskorz, P.; Komaromi, I.; Martin, R. L.; Fox, D. L.; Keith, T.; Al-Laham, M. A.; Peng, C. Y.; Nanayakkara, A.; Challacome, M.; Gill, P. M. W.; Johnson, B.; Chen, W.; Wong, M. W.; Conzalez, C.; Polple, J. A. *Gaussian 03*, revision D.01; Gaussian, Inc.: Wallingford, CT, 2004.

(31) Becke, A. D. *J. Chem. Phys.* **1993**, *98*, 5648.

(32) Lee, C.; Yang, W.; Parr, R. G. *Phys. Rev. B* **1988**, *37*, 785.

(33) Alms, G. R.; Burnham, G. R.; Flygare, W. H. *J. Chem. Phys.* **1975**, *63*, 3321.

(34) Millefiori, S.; Alparone, A. *J. Mol. Struct.* **1998**, *442*, 221.

(35) Smith, S. M.; Markevitch, A. N.; Romanov, D. A.; Li, X.; Levis, R. J.; Schlegel, H. B. *J. Phys. Chem. A* **2004**, *108*, 11063.

(36) Shinohara, H.; Yamakita, Y.; Ohno, K. *J. Mol. Struct.* **1998**, *442*, 221.

(37) Placzek, G. In *Handbuch der Radiologie*; Marx, E., Ed.; Akademische Verlag: Leipzig, Germany, 1934; Vol. 6, Part 2, p 205.

(38) (a) Long, D. A. *Raman Spectroscopy*; MacGraw-Hill: New York, 1977. (b) Yang, X.; Maeda, S.; Ohno, K. *J. Phys. Chem. A* **2005**, *109*, 7319.

(39) Klocker, J.; Karpfen, A.; Wolschann, P. *Chem. Phys. Lett.* **2003**, *367*, 566.

(40) Császár, A. G. *J. Am. Chem. Soc.* **1992**, *114*, 9568.

(41) Barone, V.; Adamo, C.; Lelj, F. *J. Chem. Phys.* **1995**, *102*, 364.

(42) Moon, S.; Kwon, Y.; Lee, J.; Choo, J. *J. Phys. Chem. A* **2001**, *105*, 3221.

(43) Sudharsanam, R.; Chandrasekaran, S.; Das, P. K. *J. Mater. Chem.* **2002**, *12*, 2904.

(44) Tachikawa, T.; Tojo, S.; Fujitsuka, M.; Majima, T. *Chem. Phys. Lett.* **2003**, *382*, 618.

(45) Hammett, L. P. *J. Am. Chem. Soc.* **1937**, *59*, 96.

(46) Hansch, C.; Leo, A.; Taft, R. W. *Chem. Rev.* **1991**, *91*, 165.

(47) Klein, E.; Lukeš, V.; Cibulková, Z.; Polovková, J. *J. Mol. Struct: THEOCHEM* **2006**, *758*, 149.

(48) Reed, A. E.; Weinstock, R. B.; Weinhold, F. *J. Chem. Phys.* **1985**, *83*, 735.

(49) Yamakita, Y.; Ohno, K. Submitted for publication.

(50) Komornicki, A.; McIver, J. W. *J. Chem. Phys.* **1979**, *70*, 2014.

JP807027Q